CP4O

CryoSat Plus for Oceans

ESA/ESRIN Contract No. 4000106169/12/I-NB

WP4000 - Progress Report on the Improvement of the Wet Tropospheric Correction for the CryoSat-2 mission

U.PORTO
FACULDADE DE CIÊNCIAS
UNIVERSIDADE DO PORTO

VERSION 1.0, 10th June 2013

Author(s)	Affiliation
M. Joana Fernandes	U.Porto & CIMAR-LA/CIIMAR-UP
Alexandra L. Nunes	IPP/ISEP & CIMAR-LA/CIIMAR-UP
Clara Lázaro	U.Porto & CIMAR-LA/CIIMAR-UP

Contents

Abbreviations and Acronyms

AMR	Advanced Microwave Radiometer (AMR)
AMSR-E	Advanced Microwave Scanning Radiometer-Earth Observing System
AMSU-A	Advanced Microwave Sounding Unit A
ATBD	Algorithm Theoretical Basis Document
CS-2	CryoSat-2
DComb	data combination (algorithm)
DMSP	Defense Meteorological Satellite Program
ECMWF	European Centre for Medium-Range Weather Forecasts
EPN	EUREF Permanent Network
ERA	ECMWF ReAnalysis
ESA	European Space Agency
EUMETSAT	European Organisation for the Exploitation of Meteorological Satellites
GDR	Geophysical Data Records
GNSS	Global Navigation Satellite Systems
GPD	GNSS-derived path delay (algorithm)
J1	Jason-1
J2	Jason-2
MWR	microwave radiometers
NASA	National Aeronautics Space Administration

NOAA	National Oceanic and Atmospheric Administration
NRL	Naval Research Laboratory (NRL)
NWM	numerical weather models
OA	Objective Analysis
PW	precipitable water
RADS	Radar Altimeter Database System
RA-MWR	MWR onboard altimetric missions
RS	remote sensing
SAR	Synthetic Aperture Radar
SI-MWR	Scanning Imager MWR
SLA	sea level anomaly
SSat	(RS) sun-synchronous satellite
SSM/IS	Special Sensor Microwave Imager/Sounder
TCWV	total column water vapour
TMI	TRMM Microwave Imager
T/P	TOPEX/Poseidon
TRMM	Tropical Rain Measuring Mission (TRMM)
U.Porto	University of Porto
WTC	wet tropospheric correction
ZWD	zenith wet delay

Acknowledgments

The authors would like to thank the European Centre for Medium-Range Weather Forecasts (ECMWF) for making available the ERA Interim data on the ECMWF data server, and all organizations which provide the water vapour products used in this study: NOAA through its Comprehensive Large Array-Data Stewardship System (CLASS), Remote Sensing Systems, the Global Hydrology Resource Center and the National Snow and Ice Data Center.

1. Scope of the document

The "Progress Report on the Improvement of the Wet Tropospheric Correction for the CryoSat-2 mission" is intended to replace the planned draft versions of the U.Porto team's contribution to the documents D4.1 – Algorithm Theoretical Basis Document (ATBD) and D4.2 – Product Validation Report. This document will report on the present status of the work being developed by U.Porto under WP4000, building on, and having as main references, the documents D2.1 – Preliminary Analysis Report, D2.2 – Development and Validation Plan, and D3.2 – Experimental Data Set User Manual. For the sake of completeness, some background information and analyses already presented in D2.1 have been also included here, and expanded with new results where applicable. Part of the work presented in this document has been submitted for publication in *Remote Sensing*.

As a result of the specificity of the product and methodologies under development, the general schedule of the sub-tasks defined within WP4000 (Product development and validation) does not apply to the computation of a wet tropospheric correction (WTC) product for the CryoSat-2 (CS-2) mission. Even though being the total time allocated to the work package suitable for attaining its final goals, WP4100 (Analysis, development and validation of the methods and algorithms) corresponds to the largest part of the team's time and effort corresponding to the whole WP4000, and is expected to be finished only by the end of July. The next step, consisting of the validation of the method against independent data sources, to be performed under WP4200, is expected to be completed by late August. This will be followed by the production of the ATBD document in its final version – WP4300 –, which shall be completed by early October. The final WTC product for CS-2, provided globally (and therefore also for the Validation Data Set to be used in WP5000) shall be finished by November and will be the main outcome of WP4400 (part of D4.3), together with the team's contribution to D4.4 - Updated Data Set User Manual. As a consequence, there will be no draft versions of D4.1 and D4.2, as these documents can only be produced once WP4100 and WP4200 are complete.

2. Introduction

With an absolute value up to 50 cm and highly variable in space and time, the path delay due to the presence of water vapour in the atmosphere, or wet tropospheric correction (WTC), is still one of the major error sources in satellite radar altimetry. Due to its high variability, the most accurate way to model this effect over open ocean is through the measurements of microwave radiometers (MWR) on board the altimetric missions.

CryoSat-2 (CS-2), primarily dedicated to measuring and monitoring the changing thickness of ice in polar regions, does not carry an onboard MWR, being the wet tropospheric correction currently applied to the radar altimeter data a model-based one, provided by the European Centre for Medium-Range Weather Forecasts (ECMWF). The more stringent accuracy requirements imposed by global-scale ocean and coastal studies, however, are driving a need to develop an improved correction for CS-2, particularly important for these applications.

As described in D2.1, a data combination (DComb) algorithm is being developed for the computation of a more accurate WTC, when compared to the one provided by ECMWF. The DComb algorithm, based on the approaches followed by [*Fernandes et al.*, 2010; *Fernandes et al.*, 2013; *Stum et al.*, 2011], estimates the WTC using objective analysis of several available data sources: scanning MWR on board remote sensing (RS) satellites, Global Navigation Satellite Systems (GNSS) and the ECMWF ReAnalysis (ERA) Interim model. A mandatory task that has to be performed in advance is the analysis and inter-calibration of these datasets for the computation of the wet path delay of altimeter measurements over open ocean, polar regions, and coastal zones, for their use in the DComb algorithm. In this context, the dataset of total column water vapour (TCWV) images acquired by the various scanning MWR on board RS missions is of particular relevance due to data amount and coverage (both in space and time) and the variety of instruments acquiring such data, which will thus require proper inter-calibration.

In the present document, the WTC computation from microwave radiometers is addressed and the main issues regarding the WTC estimation from TCWV datasets are discussed. A detailed analysis and inter-calibration of the water vapour products of scanning MWR of various sensors on board different RS missions and the main issues concerning their use and impact in the improvement of the WTC for CS-2 are discussed. In addition, in view to establish the most appropriate model for use in the DComb algorithm, a comparison between ERA Interim and the ECMWF operational model is presented. The GNSS-derived WTC has been subject to thorough analysis by the authors in the scope of previews studies, mostly in the scope of other ESA-funded projects (COASTALT and Sea Level CCI), and a brief description of the main conclusions has been provided in D2.1.

A brief status of the ongoing implementation of the DComb algorithm is presented. Finally, a summary of the main achievements and an overview of the remaining work to be performed under WP4000 are also presented.

3. WTC estimation from microwave radiometers

3.1. Introduction

The correction for the path-delay of the altimeter signal due to the presence of water vapour in the atmosphere is one of the most difficult altimeter corrections to model. The WTC is difficult to estimate because of the high variability of humidity and the complexity of the water cycle at all spatial and time scales. Mean values of WTC show a near-zonal variation, ranging from less than 5 cm at high latitudes to ~35 cm near the equator and the tropics, its standard deviation ranging from 1-5 cm near the poles to 10-15 cm in the tropics (global maps presented in D2.1, Figures 3.1.3 in D2.1).

In spite of the continuous progress in the modelling of this effect by means of numerical weather models (NWM) (e.g. [*Dee et al.*, 2011; *Miller et al.*, 2010]), accuracy of present NWM-derived WTC is still not good enough for most altimetry applications such as sea level variation. Indeed, an accurate enough modelling of this effect can only be achieved through actual measurements of the atmospheric water vapour content at the epoch and location of the altimetric measurements. For this purpose, dedicated microwave radiometers have been incorporated in the most recent altimetric missions. For simplicity, these instruments will be hereafter designated by RA-MWR, standing for nadir-looking, single measurement MWR on board radar altimeter missions.

In addition to the dedicated MWR aboard altimetric missions, scanning imaging instruments, also retrieving water vapour data from measurements in several bands of the microwave spectrum, have been flown in various RS missions. Also for simplicity, these instruments will hereafter be designated by SI-MWR, standing for scanning imaging MWR, not to be confused with the RA-MWR single-measurement systems. For the sake of completeness, the details of the instruments and water vapour products available for the various SI-MWR are presented in Section 4.

3.2. From TCWV to WTC

The total column water vapour, also referred as precipitable water, PW, or integrated water vapour, (IWV) is the total water vapour contained in an air column from the Earth's surface to the top of the atmosphere and is usually expressed in kg/m^2 or millimetres (mm), as the length of an equivalent column of liquid water.

According to [*Bevis et al.*, 1994], and as already detailed in D2.1, the *WTC* can be estimated from the total column water vapour (*TCWV*, abbreviated as WV in the following equations) and atmospheric temperature using the following expression:

$$WTC = -\left(0.101995 + \frac{1725.55}{T_m}\right)\frac{WV}{1000} \quad (1)$$

where T_m is the mean temperature of the troposphere, which may be in turn modelled from the surface temperature (T_0) according to, e.g. [*Mendes et al.*, 2000]:

$$T_m = 50.440 + 0.789\,T_0 \tag{2}$$

In Equation (1) and Equation (2), T_0 and T_m are in kelvin, *WV* in millimetres and the *WTC* results in meters. This will be hereafter called the "Bevis approach".

Alternatively, the dependence of the *WTC* on the atmospheric temperature can be implicitly accounted for by establishing a direct relationship between *WTC* and *TCWV* (e.g. [*Keihm et al.*, 1995; *Keihm et al.*, 2000; *Stum et al.*, 2011]), since the ratio between *WTC* and *TCWV* can be described by a decreasing function of water vapour content, which partly expresses the *WTC* temperature dependence. For example, in [*Stum et al.*, 2011] the following relationship was deduced from temperature and humidity profiles from ECMWF model fields:

$$WTC = -(a_0 + a_1 WV + a_2 WV^2 + a_3 WV^3)\,WV\,.10^{-2} \tag{3}$$

with a_0=6.8544, a_1=−0.4377, a_2=0.0714, a_3=−0.0038, *WV* is in cm and *WTC* results in metres.
[*Keihm et al.*, 2000] provide a similar expression which gives WTC values about 1% larger than those given by Equation (3) [*Stum et al.*, 2011]. This will be hereafter called the "Stum approach".

As part of the work developed in the scope of WP4000, both approaches, using Equation (1) and Equation (3), are considered in order to identify the most suitable for use in the WTC retrieval from SI-MWR water vapour products.

4. MWR Imaging Sensors

4.1. Data Description

For use in the WTC estimation for CryoSat-2, a database of water vapour images was set up, encompassing all scanning MWR on board RS satellites whose data are available for the period of the CS-2 mission (starting in April 2010). All information regarding SI-MWR characteristics, data and data access have been detailed in D2.1 – Preliminary Analysis Report and D3.2 – Experimental Data Set User Manual. For convenience and completeness, some of that information is repeated (and extended) in the present document. The different sensors considered are (see Tables 1 and 2):

1) the Advanced Microwave Sounding Unit A (AMSU-A) on board the National Oceanic and Atmospheric Administration (NOAA) satellite series (NOAA-15, -16, -17, -18, -19) and on board the European Organisation for the Exploitation of Meteorological Satellites (EUMETSAT) MetOp-A satellite;
2) the Advanced Microwave Scanning Radiometer-Earth Observing System (AMSR-E) on board the National Aeronautics Space Administration (NASA) Aqua satellite;
3) the Tropical Rain Measuring Mission (TRMM) Microwave Imager (TMI) on board the joint NASA and Japan Aerospace Exploration Agency TRMM satellite;
4) the Special Sensor Microwave Imager (SSM/I) and Special Sensor Microwave Imager/Sounder (SSM/IS) on board the Defense Meteorological Satellite Program (DMSP) satellite series (F15, F16, F17 and F18);
5) the WindSat Polarimetric Radiometer developed by the Naval Research Laboratory (NRL) aboard Coriolis, a satellite of the US Department of Defense.

All data are available online and can be accessed as summarised below:

1) AMSU-A Level-2 swath products are made available by NOAA through its Comprehensive Large Array-Data Stewardship System (CLASS): http://www.class.ngdc.noaa.gov. The Microwave Surface and Precipitation Products System (MSPPS) Orbital Global Data products (MSPPS_ORB) have been used. In addition, CLASS also provides similar products for SSM/I (F15), although it was found that these products are not suitable for use in the WTC computation (see sub-section 4.4).
2) For the AMSR-E, the Level-2B ocean swath (AE_Ocean) dataset was downloaded from the National Snow and Ice Data Center (ftp://n4ftl01u.ecs.nasa.gov/SAN/AMSA/AE_Ocean.002/).
3) For TMI, the Level-2 product swath dataset was acquired from the Global Hydrology Resource Center (ftp://ghrc.nsstc.nasa.gov/pub/data/tmi-op/).
4) SSM/I and SSM/IS data are available through Remote Sensing Systems (RSS) (http://www.ssmi.com/ssmi/ssmi_browse.html), which provide ocean data products for the DSMP satellites from F08 to F18. According to information on May 2013, products for F18 were not yet available. According to RSS information, after August 2006, F15 products are affected by RADCAL beacon interference. The released F15 version 7 products from RSS have been corrected for this effect. Due to the required calibration and correction, F15 version 7

products are provided with some delay; thus, for this study only data until the end of 2011 were available. In spite of the fact that RSS recommends that after August 2006 F15 products should not be used for climate studies, it will be shown in sub-section 4.4 that the corrected (version 7) RSS F15 products seem to be adequate for use in the WTC computations.

Table 1. Main characteristics of the sensors with scanning MWR images of TCWV available for this study. The scale factor of product is the value required to multiply the original product value to get the TCWV in mm. All products are swath except the last two, which are grid products. (*) Swath product from NOAA CLASS database; (**) Grid product from Remote Sensing Systems (RSS). (***) Value provided is the central pixel size (maximum pixel size is 130 km).

Sensor	Pixel size (km)	Swath width (km)	Number of (lines, pixels)	Name of product	Scale factor of product	Channels used to retrieve TCWV (GHz)
AMSR-E	9 km	1625	(variable,243)	Med_res_vapor	0.01	18.7/23.8/36.5
AMSU-A	50 km (***)	2200	(variable,30)	TPW	0.1	23.8/31.4
TMI	10 km	878	(variable,104)	Columnar_water_vapor	0.01	19.35/21.3/37.0
SSM/I (*)	25 km	1420	(variable,64)	TPW	0.1	19.35/22.235/37.0
SSM/I, SSM/IS (**)	0.25°	1790 -1850	(720,1440)	VAPOR	0.3	19.35/22.235/37.0
WindSat	0.25°	1400	(720,1440)	VAPOR	0.3	18.7/23.8/37.0

Table 2. Main orbital characteristics (compared with those of CryoSat-2) of the satellites with scanning MWR images of TCWV available for this study. Grey-shaded lines refer to gridded products and the remaining to swath products. LTAN is the Local Time of the Ascending Node. (*) CLASS products are available until present; RSS products, corrected for RADCAL beacon interference, are only available until end of 2011. (**) WindSat Version 7 of RSS products are only available until the end of 2011; after that date near real time (NRT) products are available.

Satellite	Sensor	height (km)	inclination (º)	period (min)	Sun-synch. orbit	LTAN Jan 2011 (hh:mm)	LTAN Jan 2012 (hh:mm)	data availability for CryoSat-2
CryoSat-2	-	717	92.0	93.2	No	N/A	N/A	since April 2010
Aqua	AMSR-E	705	98.0	99.0	Yes	13:36	-	until Oct 2011
NOAA-19	AMSU-A	870	98.7	102.1	Yes	13:32	13:32	until present
NOAA-18	AMSU-A	854	98.7	102.1	Yes	14:07	14:30	until present
DMSP-F15	SSM/I	850	98.8	102.0	Yes	16:44	16:05	(*)
NOAA-15	AMSU-A	807	98.5	101.1	Yes	16:35	16:35	until present
Coriolis	WindSat	830	98.8	101.6	Yes	17:54	17:54	(**)
DMSP-F17	SSM/IS	850	98.8	102.0	Yes	17:30	18:06	until present
DMSP-F16	SSM/IS	845	98.9	101.8	Yes	19:12	18:30	until present
NOAA-17	AMSU-A	810	98.7	101.2	Yes	20:20	19:40	until present
NOAA-16	AMSU-A	849	99.0	102.1	Yes	19:16	20:00	until present
MetOp-A	AMSU-A	817	98.7	101.4	Yes	21:26	21:27	until present
TRMM	TMI	402	35.0	93.0	No	N/A	N/A	until present

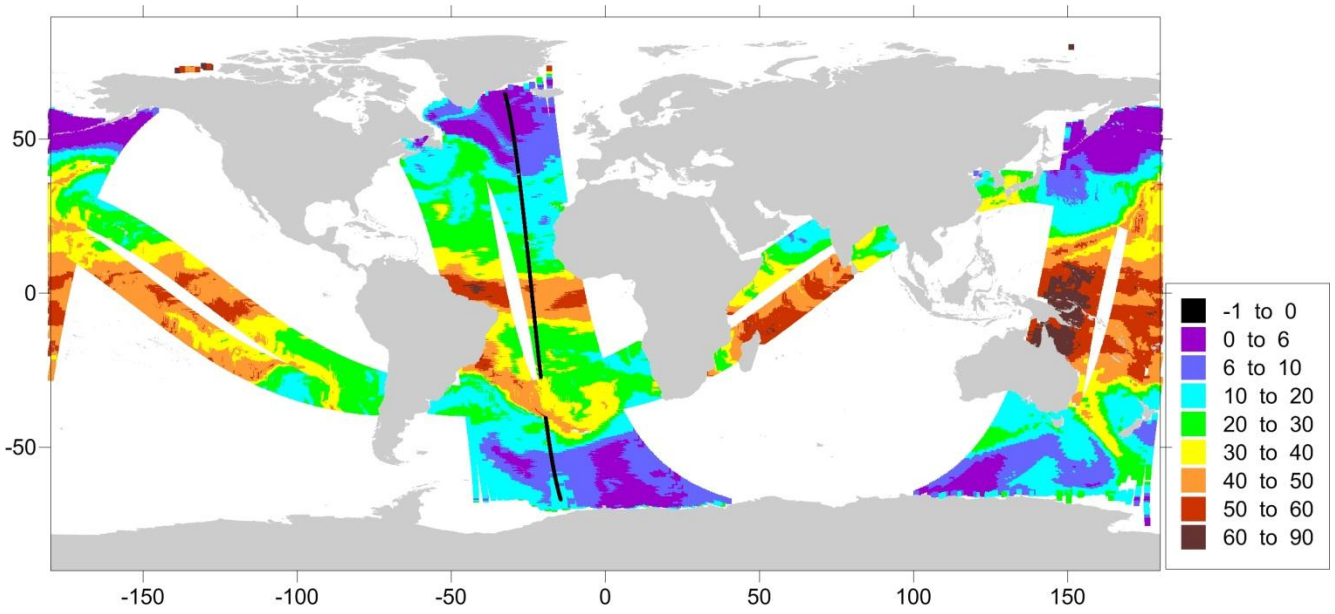

Figure 1. NOAA-17 (AMSU-A) and TRM (TMI) images closest in time to CS-2 ascending pass 3 (in black), sub-cycle 26 (March 16, 2012). Colour scale is TCWV in mm.

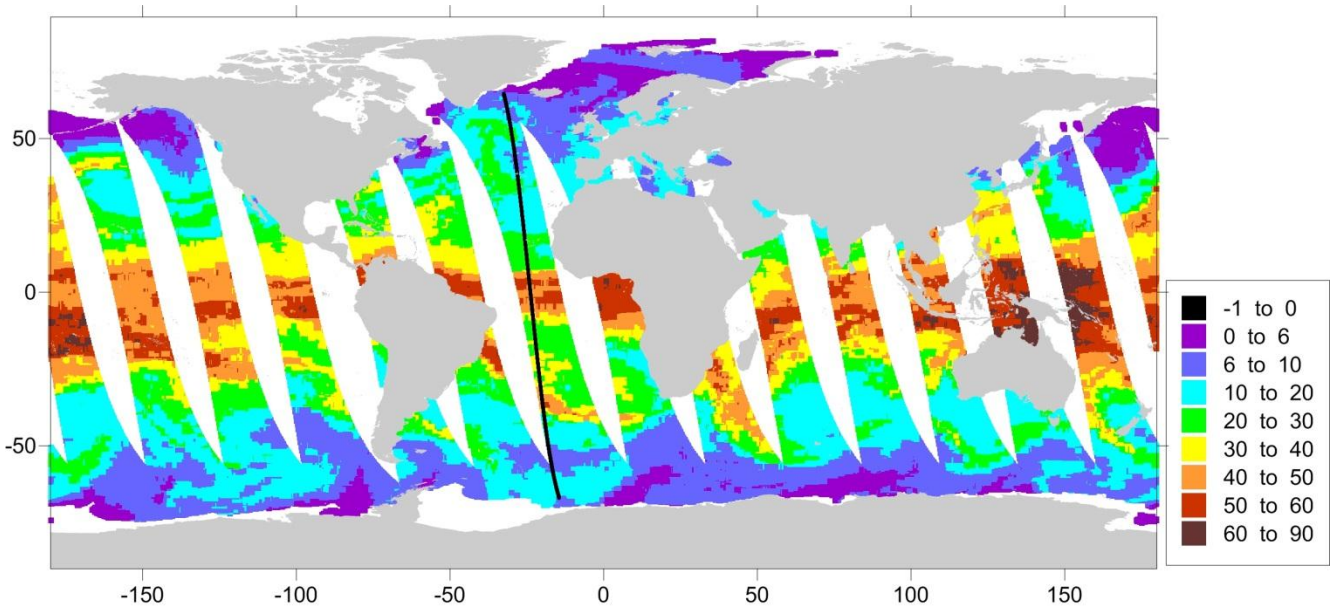

Figure 2. Coriolis (WindSat) ascending images for the same day of CS-2 ascending pass 3 (in black), sub-cycle 26 (March 16, 2012). Colour scale is TCWV in mm.

5) WindSat data are available through RSS (ftp://ftp.remss.com/windsat) also in the form of grid binary files; as for DMSP-F15 (see point 4 above) WindSat version 7 products are being generated with some delay, and for the present study they were only available until the end of 2011 - for the remaining period the near real time products are available. RSS also provides similar gridded products for AMSR-E.

Two types of water vapour products containing the TCWV field have been used: 1) Level-2 swath products, whenever available, from all data providers except RSS; 2) Level-2 gridded products, otherwise (from RSS). Swath products are available in HDF-EOS2 format, while gridded products are available in binary format. The existing products and their main characteristics are summarised in Table 1 and Table 2 (status as in February 2013). Figures 1 and 2 show examples of the swath and gridded products, respectively.

4.2. Orbit Configuration

In this section we present an analysis of the characteristics of the orbits of the satellites providing the SI-MWR images and compare various orbital parameters with those of CryoSat-2, in view to understand the type of coverage that can be expected for CS-2 from these images.

When examining Table 2, the first remark is that, except for TMI, all MWR scanning sensors are on board satellites with sun-synchronous orbits with an inclination (98°-99°) close to that of CS-2 (92°). This means that the local time of ascending node (LTAN) of each satellite remains constant all over the year. On the contrary, since CS-2 orbit is not sun-synchronous, and with a very long repetition cycle (369 days), every day the satellite will have a pass over a different location and the corresponding LTAN will change accordingly. This means that the set of RS satellites that provide good space-time coverage for CS-2 at a given epoch, or, say, are in phase with CS-2, will be out of phase a few months later, with a large time difference between the acquisition time of the corresponding images and the CS-2 passage.

According to Table 1, and not considering the AQUA satellite -- since AMSR-E stopped working on October 4, 2011 --, there are 10 RS missions in near polar sun-synchronous orbits providing water vapour products: NOAA-15, -16, -17, -18, -19, MetOp-A, DMSP-F15 (with some restrictions), -F16, -F17 and Coriolis. In summary, since October 2011 there is a total of 11 satellites (now including the non-sun-synchronous TRMM), with five different MWR scanning sensors with variable pixel size: 50 km, 25 km and 10 km for nadir looking (see Table 1).

It was already mentioned that CS-2 has a very long repetition cycle of 369 days. For practical reasons, a convention was established and has been used by RADS (Radar Altimeter Database System) with the purpose of dividing the long 369-day cycle of CS-2 into shorter periods, guaranteeing that collinear tracks (that is, 369 days apart) have the same pass number and that passes with the same number (within each sub-cycle of a full CS-2 cycle) are close together. Therefore, each CS-2 cycle is divided into 13 sub-cycles of 29 or 27 days, as follows: four repetitions of three sub-cycles of 29, 29 and 27 days, plus an additional sub-cycle of 29 days (i.e., $4\times(29+29+27) + 29 = 369$ days). The same convention was adopted in this study.

In order to compare the orbit of each sun-synchronous satellite with that of CS-2, the longitude of equator crossings (ascending and descending), here referred as Lon_Node, and corresponding epochs were determined for CS-2 and all 11 sun-synchronous satellites mentioned above. Figure 3 shows Lon_Node versus time, at middle of CS-2 sub-cycle 17 (July 2011), for a period of two days. It can be observed that the time distribution of the SI-MWR images is not uniform throughout the day, the maximum time difference between two images being around 4 hours (between an ascending MetOp-A

and a descending NOAA-19 image or vice-versa). A similar analysis for other CS-2 sub-cycles demonstrates how different the space-time coverage of the SI-MWR images is for different times of the year and, therefore, throughout the CS-2 mission.

The variation of CS-2 orbit with respect to each sun-synchronous satellite can also be inspected in Figure 4, which represents the time evolution of the LTAN and local time of descending node (LTDN) of all 11 sun-synchronous RS satellites and of CS-2 passes from middle of sub-cycle 11 (February 2011) to middle of sub-cycle 35 (December 2012).

Using the theory of satellite orbit perturbations it can be shown that the CS-2 orbital configuration repeats with respect to a pure sun-synchronous orbit with a period of ~482 (482.52) days (the time that takes the CS-2 orbital plane to perform a full revolution with respect to the Sun). Therefore, the coverage observed in the examples shown in Figure 3 repeats every 482 days. This is also clearly illustrated in Figure 4.

In addition to the fact that CS-2 orbit varies with respect to the corresponding orbits of the sun-synchronous satellites, the LTAN of the latter may also drift in time, in particular for the oldest missions (e.g. [*Ignatov et al.*, 2004]). This is illustrated in Figure 4 and also in Table 2, where the approximate LTAN of the various satellites is given for two epochs one year apart.

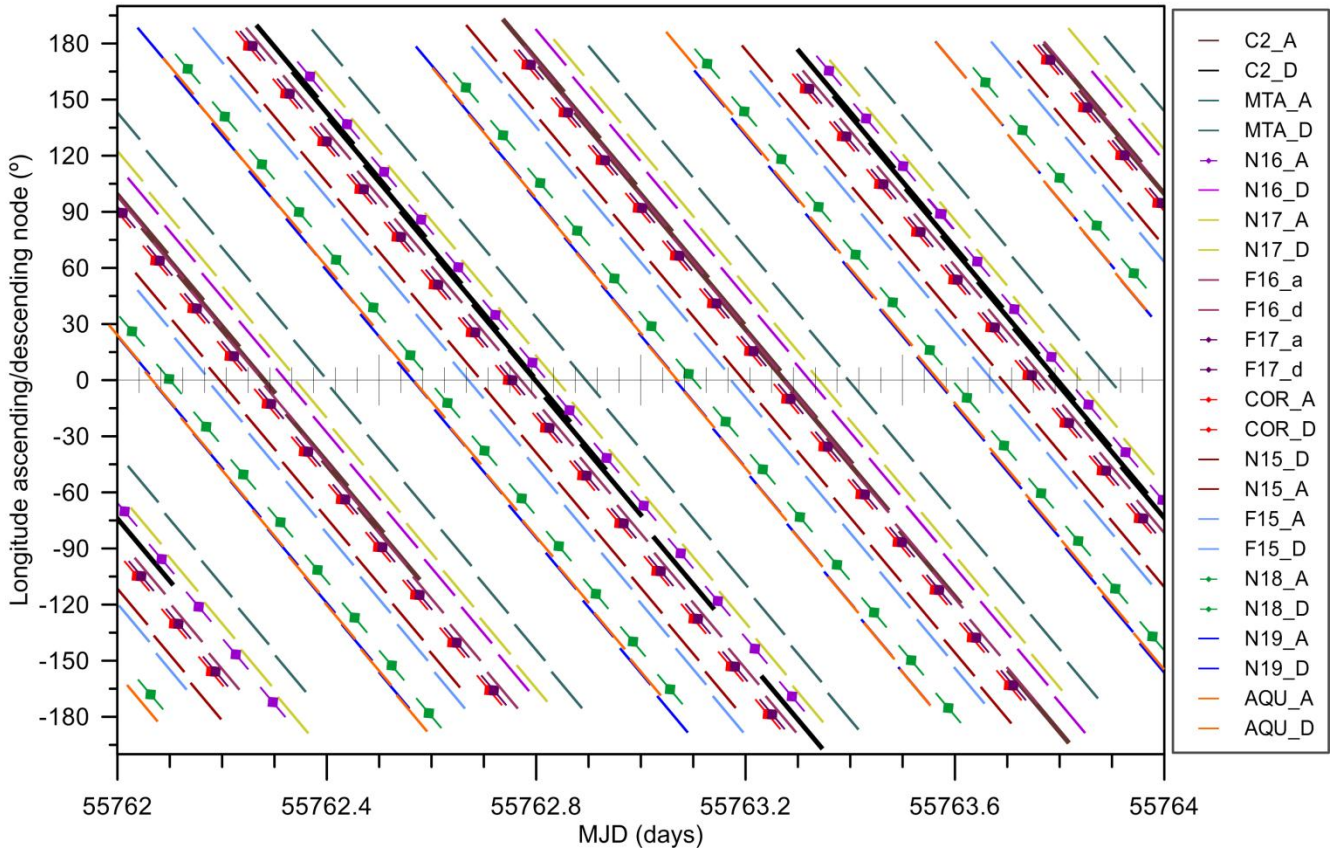

Figure 3. Longitude of equator crossings (Asc. and Desc.) versus time, at middle of CS-2 sub-cycle 17 (July 2011), for all 11 sun-synchronous RS satellites.

Results show that the most favourable conditions occur in the following two cases:

1) When an ascending CS-2 pass is in phase with an ascending pass of the RS satellite which is collecting the SI-MWR images, i.e. both satellites have close LTAN and close LTDN, since both passes are nearly parallel. This happens for the middle of CS-2 sub-cycle 26 and satellites Coriolis, F16 and F17 (Figure 4).
2) When an ascending CS-2 pass is in phase with a descending pass of the RS satellite, i.e. the CS-2 LTAN is close to the LTDN of the sun-synchronous satellite, or vice-versa, when a fraction of the SI-MWR images will be within an acceptable space/time range for the WTC computation. This happens for the middle of CS-2 sub-cycle 18 and satellites Coriolis, DMSP-F16 and -F17 (Figure 4).

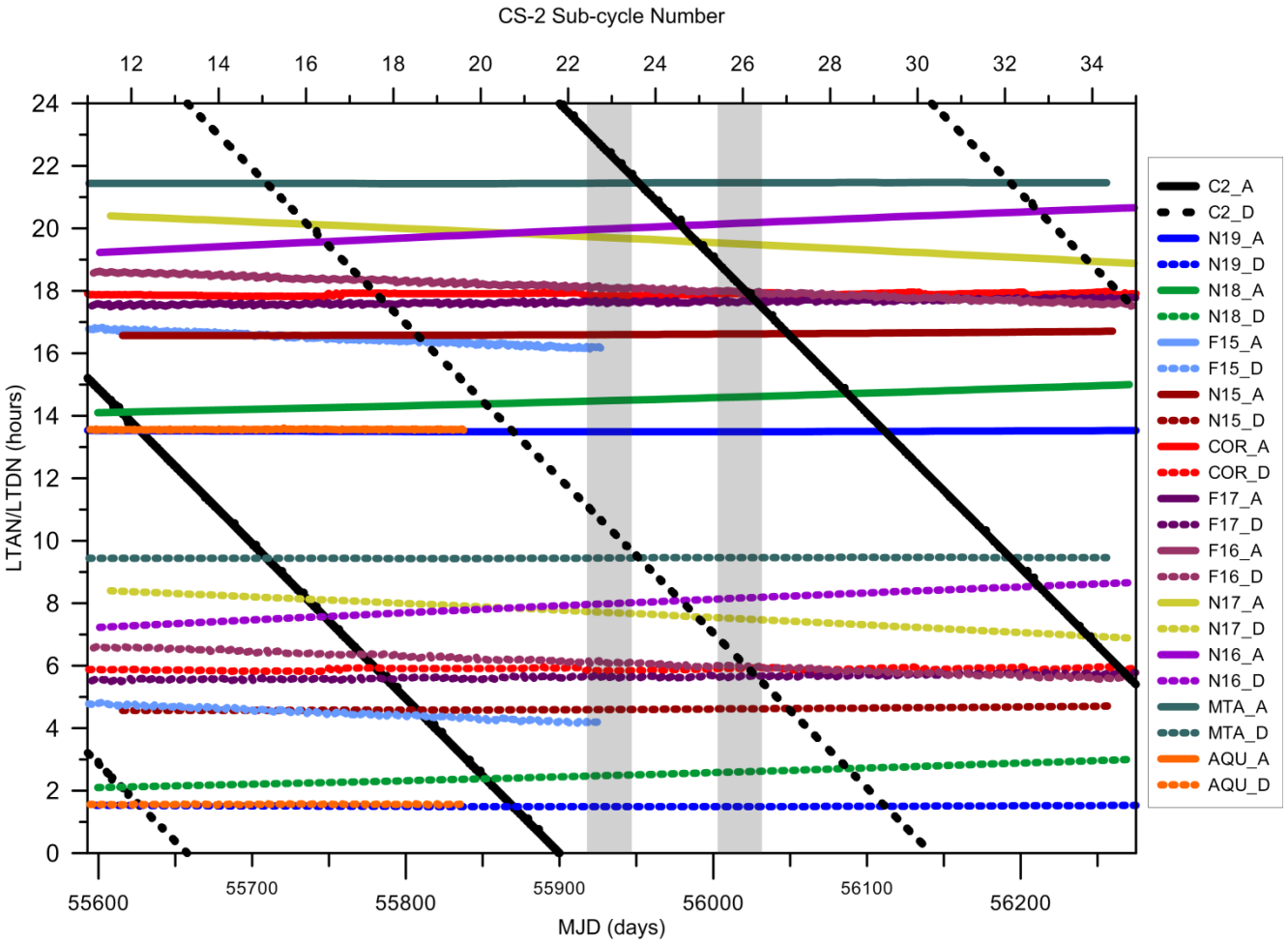

Figure 4. Time evolution of the local time of ascending node (LTAN, solid lines) and local time of descending node (LTDN, dashed lines) of all 11 sun-synchronous RS satellites and of CS-2 passes from middle of sub-cycle 11 (February 2011) to middle of sub-cycle 35 (December 2012) The vertical grey bars highlight cycles 23 and 26, which are representative of extreme conditions for CS-2 coverage.

Concerning TRMM, since its orbit is not sun-synchronous and with an inclination of 35°, each CS-2 pass will always cross a TRMM pass within two hours, in the latitude band ±40° (Figure 1). Therefore, in this latitude band, a portion of each CS-2 pass will always have TMI images available.

4.3. Spatial and temporal coverage with respect to CryoSat-2

In this section we examine how the space-time coverage of the SI-MWR images varies during the CryoSat-2 mission and how this will affect the WTC estimation for CS-2.

In order to estimate the number of images available for the computation of the WTC for each CS-2 sub-cycle, the number of different images available for each CS-2 point along the satellite track was computed, considering different values for the time difference (ΔT) and distance (ΔD) between each CS-2 point and each image satisfying these conditions (indeed between the CS-2 point and the closest point (centre of pixel) in each image).

This is illustrated in figures 5 and 6 for sub-cycles 23 and 26, respectively, chosen as representative of the extreme conditions that can occur. In this analysis, only one every 30 CS-2 points were analysed (to save computation time) and various values were considered for ΔT and ΔD. For each SI-MWR image, only points with valid TCWV values were considered. The results are summarised in Table 3 and Table 4, for sub-cycles 23 and 26, respectively.

Figures 5 and 6 resulting from this analysis show that, as expected, the number of images available for the computation of the WTC increases with latitude, in the same way as the percentage of image overlaps (see Figures 1 and 2). Due to its low inclination, TRMM has a clear impact in the coverage of the low latitudes, in the band ±40° (Figure 1).

As the previous analysis, illustrated by Figures 5 and 6, has shown, the number of images available within a certain time interval is not uniform throughout the year. Sub-cycles 23 (January 2012) and 26 (April 2012) are representative of the less and the most favourable conditions, respectively. Considering these results, the time difference ΔT has a larger effect in the coverage than the distance ΔD. For sub-cycle 26, most of the altimeter ground-track points for which the number of available SI-MWR images is zero (N_0) are either at coastal areas or at high latitudes (Figure 9). Apart from these regions, full coverage is obtained within 2 hours for this sub-cycle. It can be concluded that the distance ΔD has a clear impact in the coastal regions. Comparing analysis for the same ΔT and different ΔD (not shown here) it can be observed that a decrease in ΔD augments the number of coastal points with no SI-MWR images available. For sub-cycle 23, there are still about 10% of the altimeter ground-track points without any SI-MWR image within range, even when considering a time difference ΔT of 3 hours.

Table 3. Percentage of points with zero available images (N_0) for CryoSat-2 sub-cycle 23 as function of ΔT and ΔD. The main contribution is from 5 different satellites: MetOp-A, NOAA-16, -17, and -19 and TRMM.

ΔT \ ΔD	50 km	75 km	100 km
60 min	65.2	62.5	61.3
90 min	54.0	50.7	49.2
120 min	39.9	36.2	34.6
150 min	24.9	21.3	19.8
180 min	13.6	10.2	9.0

Table 4. Percentage of points with zero available images (N_0) for CryoSat-2 sub-cycle 26 as function of ΔT and ΔD. The main contribution is from 8 different satellites: NOAA-15, -16, -17 and -19, Coriolis, DMSP-F16 and -F17 and TRMM.

ΔT \ ΔD	50 km	75 km	100 km
60 min	8.9	7.2	6.6
90 min	2.9	2.0	1.6
120 min	1.0	0.5	0.3
150 min	0.9	0.4	0.3
180 min	0.8	0.3	0.2

Having analysed two sub-cycles representative of the most and less favourable conditions and knowing that the coverage is function of latitude, the percentage of CS-2 points with zero SI-MWR images available (N_0) and the mean number of images available within a certain region (N_m) was computed for two latitude bands: ±5° and in 40°-50°, using ΔD=75 km and three values for ΔT (90 min, 120 min and 180 min). Results are illustrated in figures 7 and 8 respectively.

These figures confirm the results already presented and give a clear indication of the variation of the space-time coverage of the set of SI-MWR images with respect to CS-2. It can be observed that the same conditions repeat every 241 days, the time that takes and ascending/descending CS-2 pass to be in phase with an ascending/descending pass of each sun-synchronous satellite. For example, considering a time interval of 3 hours both near the equator and at latitude 45°, the percentage of N_0 values varies from 0% to about 15%. In the equator, the mean number of images N_m varies from 0 to 5 while at latitude 45° it varies from 2 to 6. Decreasing the time difference ΔT will change these numbers accordingly. Since the orbital period of each satellite is about 100 minutes (see Table 2) the critical value for the time difference ΔT is about 120 min. However, for epochs such as for sub-cycle 23, increasing ΔT from 120 minutes to 180 minutes considerably increases the number of images available, reducing N_0 from 36% to 10%, for ΔD = 75 km.

In summary, globally the SI-MWR images constitute a very valuable dataset for the WTC computation for CS-2. While for most of the time these images assure a nearly full coverage within three hours, for certain periods of the CS-2 mission the coverage of these images will be insufficient for the computation of an accurate wet tropospheric correction. This stresses the importance of the remaining datasets to be used in the data combination algorithm: GNSS and ERA Interim model derived WTC.

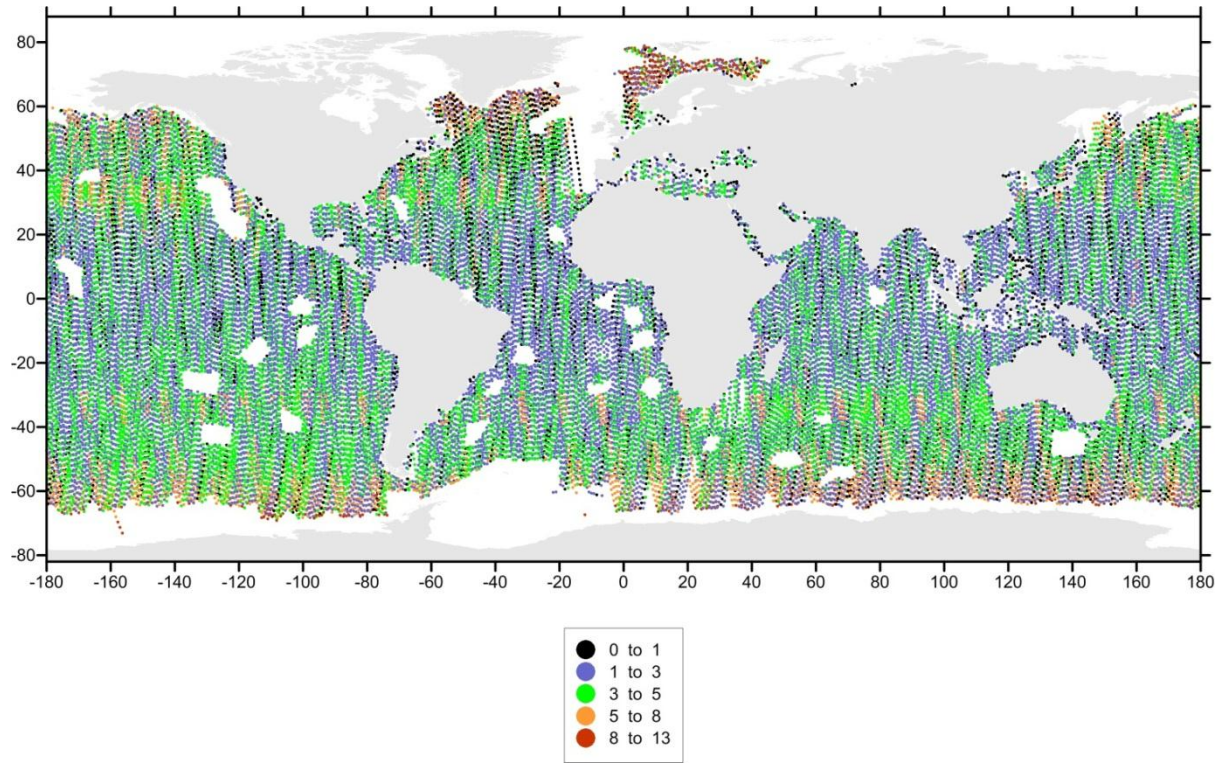

Figure 5. Number of images available for each CS-2 point, for sub-cycle 23 (January 2012), using ΔT = 180 min and ΔD = 75 km. The points with N=0 (10.2 %) are shown in black. DMSP-F15 images were not considered.

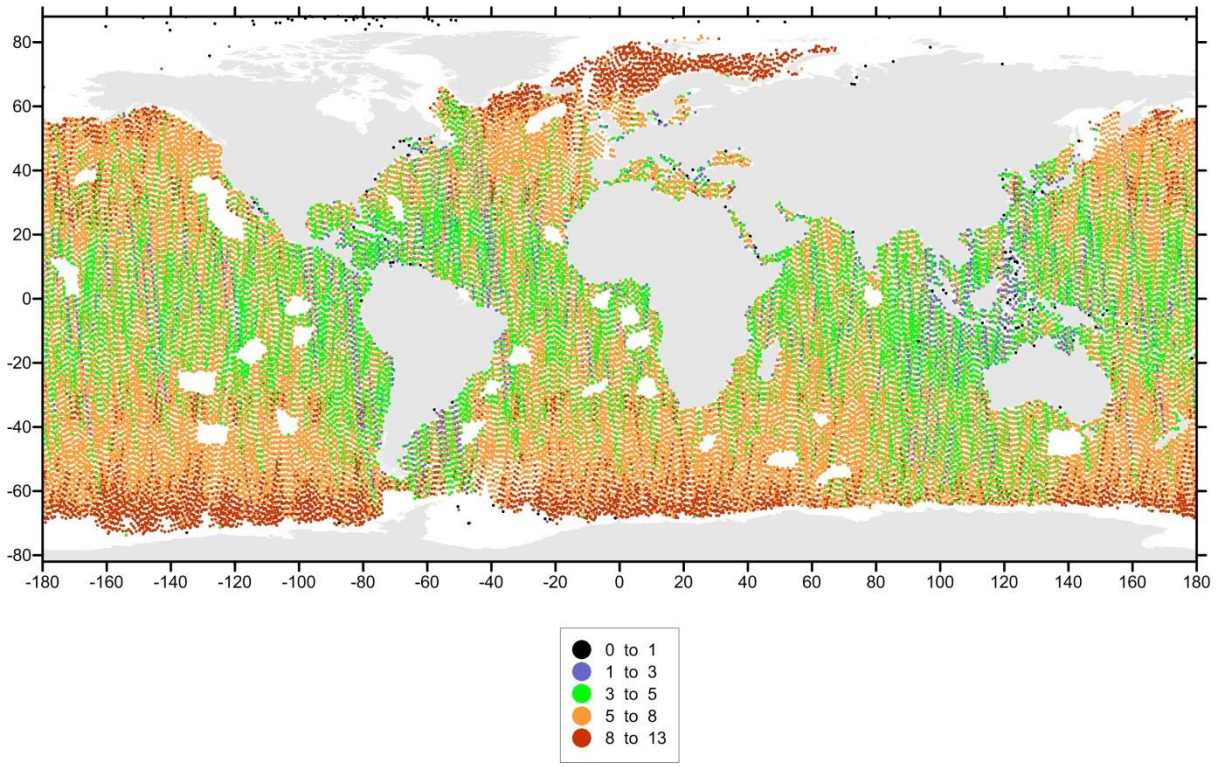

Figure 6. Number of images available for each CS-2 point, for sub-cycle 26 (April 2012), using ΔT = 180 min and ΔD = 75 km. The points with N=0 (0.3 %) are shown in black. DMSP-F15 images were not considered.

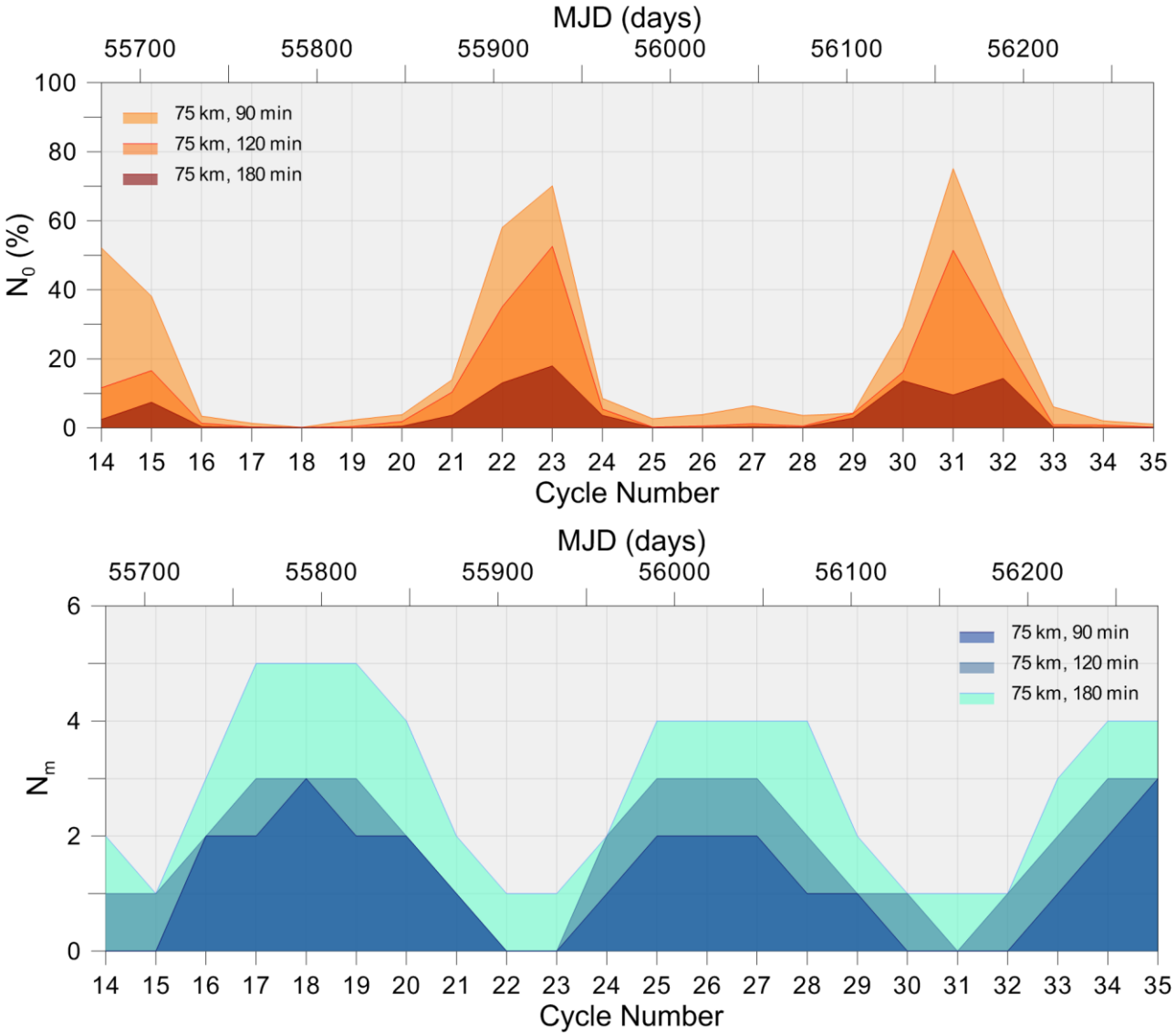

Figure 7. Percentage of points with zero available images (N_0) for CryoSat-2 sub-cycles 11 to 35 for ΔD =75 km and three different values of ΔT (top) and mean number of available SI-MWR images for each CS-2 measurement point (bottom) in the latitude band ±5°. All 12 satellites in Table 2 were used.

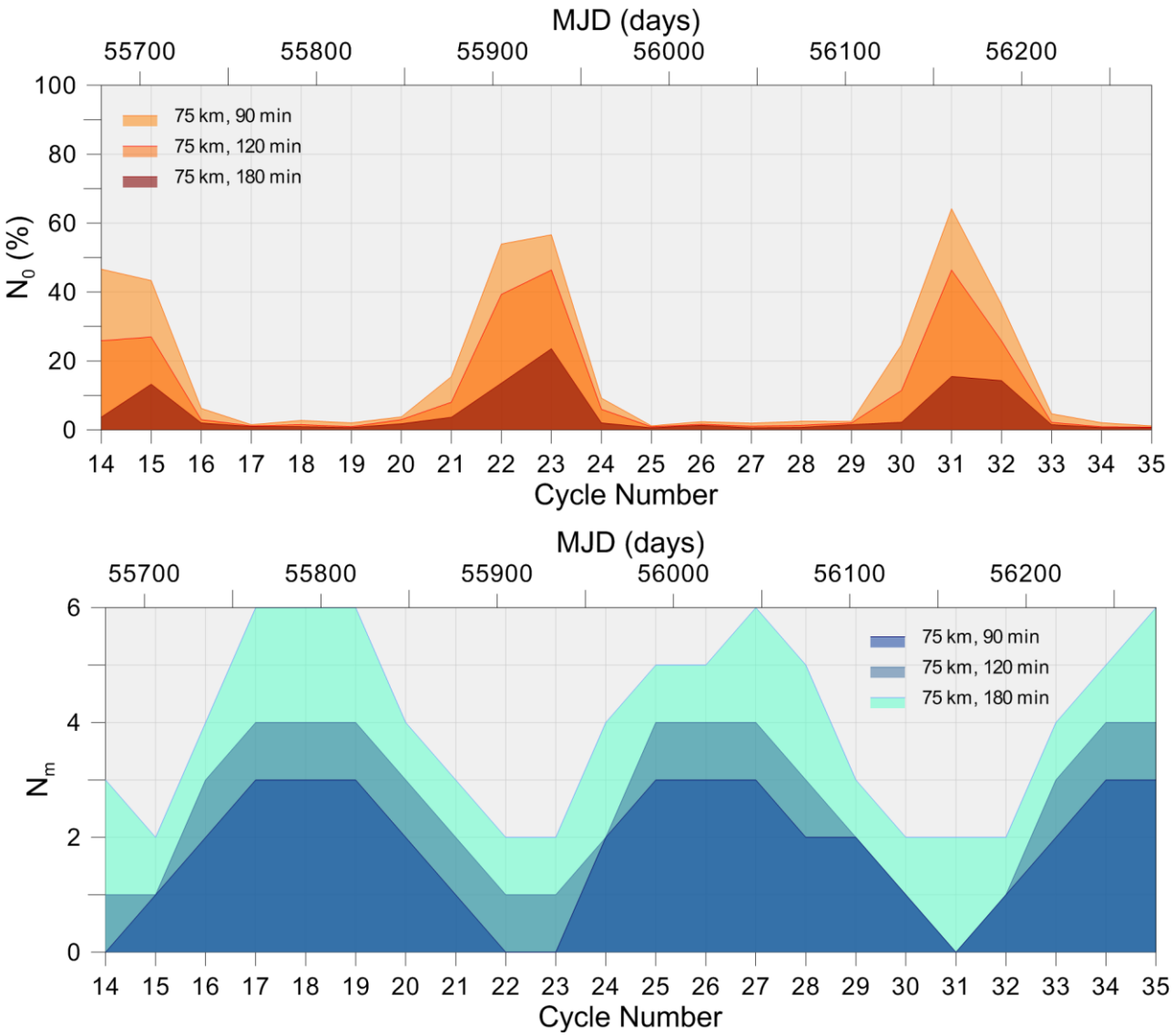

Figure 8. Same as on Figure 7 for the latitude band 40°-45°. All 12 satellites in Table 2 were used except for TMI, since this sensor only covers the region between ±40°.

4.4. Sensor Calibration

To prepare the SI-MWR TCWV data from all available MWR imaging sensors for use in the WTC computation, all datasets must be calibrated with respect to a common reference. For this purpose, the WTC retrieved by the Advanced Microwave Radiometer (AMR) on board Jason-2 (J2) was used. The reason for adopting AMR is due to the fact that this radiometer has been well monitored and the subject of successive calibrations (e.g. [*Brown*, 2013]). In order to maintain its long-term calibration, AMR was subject of a dedicated inter-satellite calibration with respect to Aqua/AMSR-E, TRMM/TMI and DMSP-F16/SSMIS for a period of three years. In the scope of this inter-calibration process, both latitudinal and different viewing geometry (nadir RA-MWR vs. non-nadir SI-MWR observations) biases were taken into account and corrected for, being the resulting calibrated AMR data and products included on the GDR-D (Geophysical Data Records) version of Jason-2 data [*Brown*, 2013]. An

absolute standard is not yet available for microwave radiometers (e.g. [*Cao et al.*, 2011]), and even though it is known that AMR does have unresolved stability issues and could, therefore, be avoided as a reference, having been carefully recalibrated against reference microwave sensors, makes it itself an acceptable common reference within the present work.

For the calibration of each SI-MWR derived WTC, a dataset of observations collocated with AMR, i.e., located within a specified space and time interval around the AMR observation, was built. Each collocation is generated by a pair of J2 and SI-MWR sensor observations, provided they occur within 50 km and 45 min of each other. For each AMR ground-track point, the closest SI-MWR image point within the given time interval was selected. In this way, a database of collocations is generated for each MWR imaging sensor.

Using the theory of orbit perturbations, it can be proven that for each RS sun-synchronous satellite (SSat), J2/SSat orbital configurations repeats once every 118 (117.45) days (~12 J2 cycles). This is illustrated in Figure 9 which represents the time evolution of the LTAN (solid lines) and LTDN (dashed lines) of all sun-synchronous RS satellites and of J2 cycles from middle of J2 cycle 108 (June 13, 2011) to middle of J2 cycle 132 (February 6, 2012).

Considering that the inclination of each sun-synchronous satellite is greater than 90° and that of J2 is less than 90° (66.4°), the number of J2/SSat collocated points is maximum when an ascending SSat pass is in phase with a descending J2 pass and vice-versa, which happens once every 118 days (~12 J2 cycles). For example, considering Coriolis, this happens for J2 cycles 108, 120 and 132 represented in Figure 9. For TMI, the J2/TRMM orbital configurations repeat once every 78 (77.76) days (~ 8 J2 cycles).

To inspect how the calibration parameters depend on the chosen dataset, for Coriolis/WindSat the collocation points and corresponding calibration parameters were computed for a large set of J2 cycles (61 to 156) covering a period of about 2.5 years. It can be observed that the number of collocations and their geographical locations have strong time dependence, as already mentioned above. This is well illustrated in Figure 10, in which the location of collocated J2/Coriolis points for three J2 cycles is shown. The time variation of the number of collocated points for J2/AQUA and J2/TRMM was also reported by [*Brown*, 2013].

The bottom panel of Figure10 shows (in green) the collocations for J2 cycle 132, for which the time of J2 LTAN coincides with the Coriolis LTDN (see also Figure 9), the most favourable configuration for getting the largest possible number of collocations, spanning the whole latitude range. In this case the passes of both satellites are nearly parallel, although they are moving in opposite ways. The top panel of Figure 10 represents, in blue, the collocations for J2 cycle 138, for which the J2 LTAN coincides with the Coriolis LTAN, that is, the ascending passes of both satellites occur within the accepted time range but they intercept at a large angle, due to the different inclination of the respective orbits. In this case, a considerable number of collocations is obtained but only for the lowest latitudes. Finally, the top panel of the same figure also shows, in red, the collocations for J2 cycle 135. This represents the typical situation for all J2 cycles which occur between the two configurations described above, in which only a small number of collocations is obtained, all at high latitudes, therefore sampling only the water vapour conditions of these regions, not representative of the whole range of TCWV values.

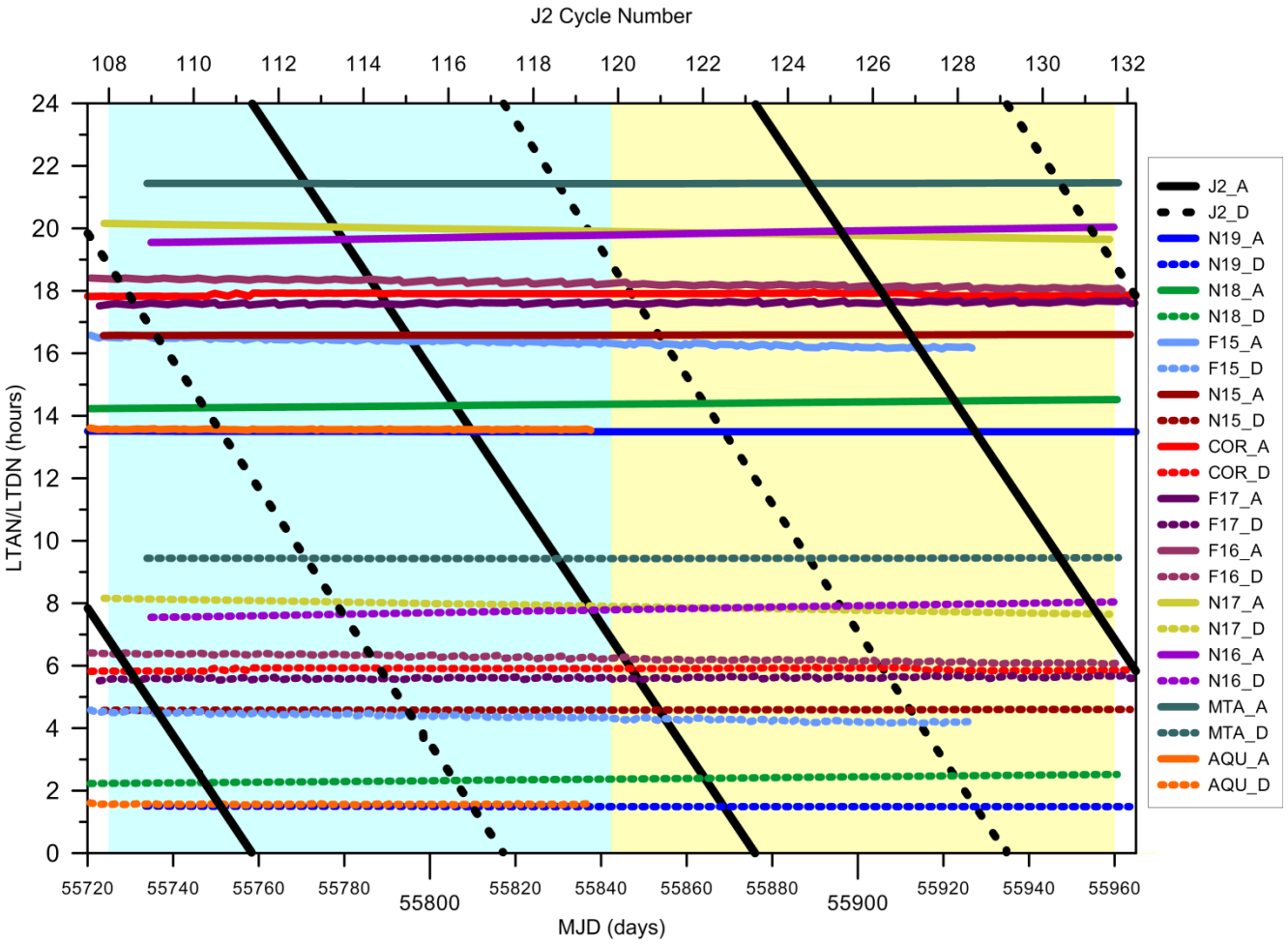

Figure 9. Time evolution of the LTAN (solid lines) and LTDN (dashed lines) of all sun-synchronous RS satellites and of J2 cycles from middle of J2 cycle 108 (June 13, 2011) to middle of J2 cycle 132 (February 6, 2012). Background colours highlight periods of 12 J2 cycles (~120 days).

The calibration parameters determined for Coriolis/WindSat and each J2 cycle (61 to 156), covering a period of about 2.5 years, were analysed. It was found that the estimated parameters reveal a small seasonal signal. Therefore, to get stable parameters it is important to use a number of J2 cycles over at least the period of one year, covering the main seasonal variations of the water vapour in the atmosphere.

In summary, for calibration purposes, a set of J2 cycles with a J2/SSat configuration of the first type described above (Figure 10, bottom panel) shall be selected, covering at least the period of one year.

For each SI-MWR dataset several J2 cycles were selected, separated at intervals of 78 days (for TRMM) and 118 days (for all sun-synchronous satellites) and covering the period of about one year. For example, the set of J2 cycles used in the calibration of Coriolis/WindSat were: 61, 73, 85 and 97.

For all collocated points of the whole set of SI-MWR sensors, the WTC was derived from the TCWV products using 1) the formulation presented by [*Bevis et al.*, 1994], Equation (1), -- the "Bevis approach" --, and 2) the formulation proposed by [*Stum et al.*, 2011], Equation (3) – the "Stum approach". In addition, the WTC from ERA Interim fields was also computed according to Equation (1) for the location and epoch of the collocated points of each database (those of J2). In this way, three

WTC datasets were computed. In the subsequent analysis, instead of the negative WTC values, the corresponding symmetric (positive) wet path delay values were used. This approach was adopted to facilitate the illustration of the results, both in terms of the calibration plots and associated calibration parameters. The three wet path delays (WPD) datasets calculated this way for each database of collocated points are designated by WPD_Bevis, WPD_Stum and WPD_ERA, respectively, and were plotted against the corresponding WPD from AMR (WPD_AMR). We recall that WPD_AMR is the symmetric of the WTC correction retrieved from AMR GDR-D products, present in RADS.

For every satellite/sensor, a linear fit was computed for each of the three datasets (WPD_Bevis, WPD_Stum and WPD_ERA) against WPD_AMR, and the calibration coefficients, i.e. scale factor and offset, were thus derived from the obtained parameters.

Figures 11 and 12 illustrate the results for Coriolis/WindSat images, while Figures 13 and 14 show the corresponding results for MetOp-A/AMSU-A.

Table 5 shows the calibration parameters (scale factor and offset) for all 12 analysed SI-MWR for both WPD_Bevis and WPD_Stum. In addition to the calibration parameters, the statistical parameters of the differences between WPD_AMR and WPD_Bevis or WPD_Stum before and after applying the calibration parameters were computed and are also shown in Table 5.

Results show that, before calibration, WPD_Stum underestimates the wet path delay by 1.2-3.2% while WPD_Bevis overestimates the WPD by 0.1-2.0% (Figures 11 to 14 and Table 5). After calibration, i.e. after applying the derived scale factors and offsets, WPD_Bevis and WPD_Stum agree within ± 2mm.

Figures 12 and 14 illustrate that AMR is well calibrated with respect to ERA Interim and that both the WPD retrieved using the Bevis and Stum approaches agree very well with ERA Interim, although, on average, the calibration coefficients for the Bevis approach are closer to those obtained for ERA Interim. It should be recalled that AMR has been calibrated with respect to ECMWF operational model, which, since 2004, is very similar to ERA Interim (see section 5) and [*Brown*, 2013]).

Although AMR is well calibrated with respect to ERA Interim, the RMS (Root-Mean Square) of the differences between WPD_AMR and WPD_ERA after calibration has values in the range 1.3-1.6 cm for all satellites, which evidences the lower accuracy of this model when compared to the various SI-MWR. This is also illustrated in Figures 12 and 14, which show a larger spread of WPD_ERA compared to WPD_Bevis with respect to WPD_AMR.

Results presented in Table 5 show that, overall, all SI-MWR are well calibrated with respect to AMR. For some of these sensors these results were expected since, as mentioned above, AMR has been calibrated with respect to TMI, AMSR-E and F15-SSM/IS [*Brown*, 2013].

The fact that the obtained calibration parameters for these satellites are not exactly 1.0 for the scale factor and 0.0 for the offset can be attributed to the following different aspects of the presented methodology: (1) different datasets for AMSR-E and F15-SSM/IS were used (swath versus grid products); (2) possible latitudinal biases were not taken into account; (3) no restrictions were imposed to, or effect corrected for, the viewing geometry of the SI-MWR observations used, what may help explaining the slight overestimation/underestimation of the SI-MWR-derived WTC using the Bevis and Stum approaches, respectively, before calibration.

For the period of time considered, the best results for RMS of the differences between the WTC derived from AMR and the corresponding values derived from each imaging sensor using the Stum approach and after calibration are (in cm): Coriolis/WindSat (0.80) and AQUA/AMSR-E (0.86). All

DMSP satellites' sensors (F15 (from RSS), F16 and F17) have an RMS of 1.0 cm. For all other sensors (on board TRMM, NOAA-15, -16, -17, -18, -19, MetOp-A, the corresponding RMS with respect to AMR, after calibration, are in the range 1.1-1.2 cm (Table 5)). The corresponding RMS differences for the Bevis approach are systematically larger but only by very small values, all less than 1 mm. In face of these results, WPD_Stum agree with the values derived from AMR slightly better than WPD_Bevis, In practice and for this type of application, the two methods give equivalent results, with differences below the accuracy level of the WTC estimation.

Following the information referred in section 4.1, the use of DMSP-F15 SSM/I data after August 2006 had to be subject to some prior analysis. Therefore, the latest available version of such data was analysed, by comparing the derived WTC with that of AMR. Results show that DMSP-F15 SSM/I data from RSS have a performance very similar to those of -F16 and -F17 SSM/IS, being therefore appropriate for use in this study (Table 5, Figures 15 and 16.). On the contrary, DMSP-F15 SSM/I swath products provided by NOAA CLASS system reveal a serious degradation for that period, evidencing that this dataset has not been corrected for the mentioned anomalies.

The calibration parameters presented in table 5 refer to wet path delay values. The corresponding parameters to be applied to WTC values are related to those on table 5 as follows: scale factor – the same; offset – multiply those on Table 5 by (-1).

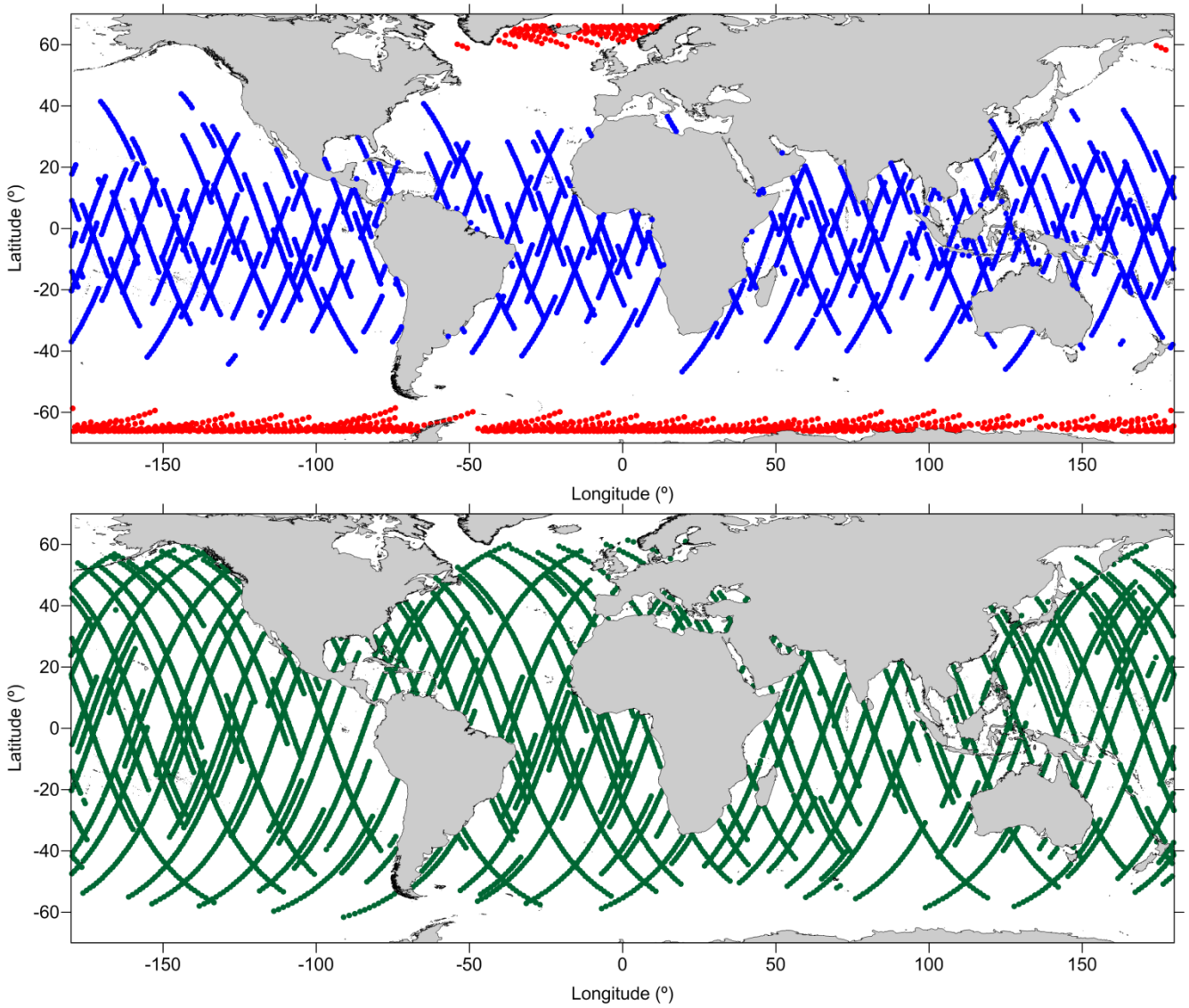

Figure 10. Location of collocated Coriolis(/WindSat)/AMR points for J2 cycles 132 (bottom, in green), 135 (top, in red) and 138 (top in blue).

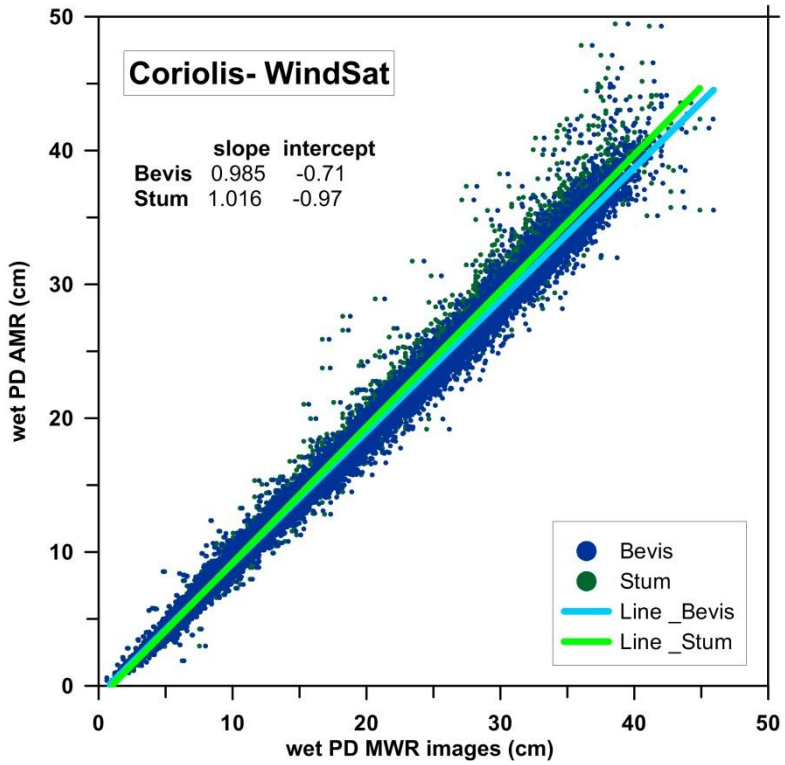

Figure 11. Wet path delay from AMR versus the corresponding values from Coriolis/WindSat using the Bevis (blue) and the Stum (green) approach. The solid lines represent the linear fit to each dataset.

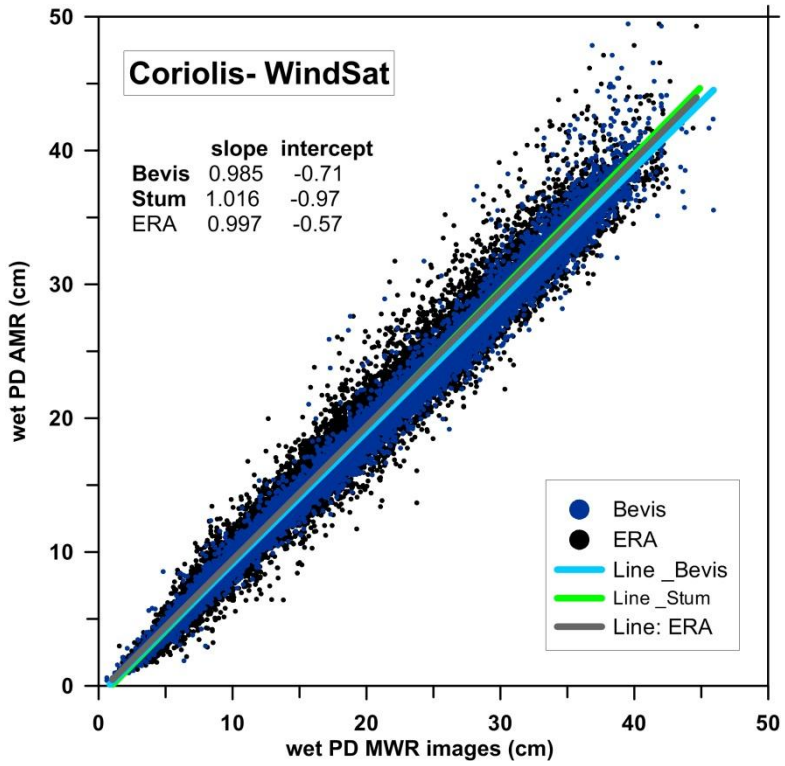

Figure 12. Wet path delay from AMR versus the corresponding values from Coriolis/WindSat using the Bevis approach (blue). In black the corresponding values from ERA Interim. The solid lines represent the linear fit to each dataset.

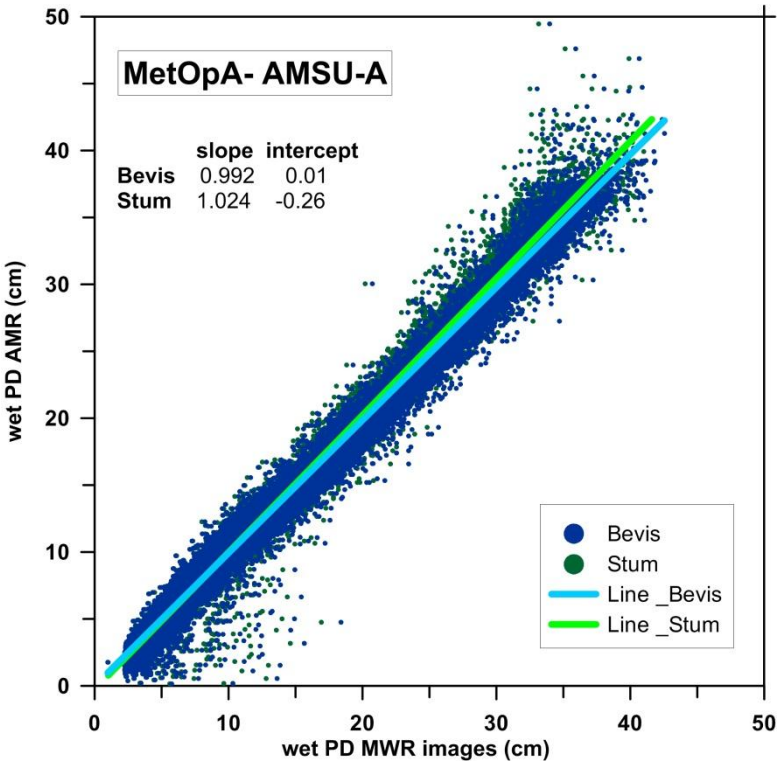

Figure 13. Wet path delay from AMR versus the corresponding values from MetOp-A/AMSU-A using the Bevis (blue) and the Stum (green) approach. The solid lines represent the linear fit to each dataset.

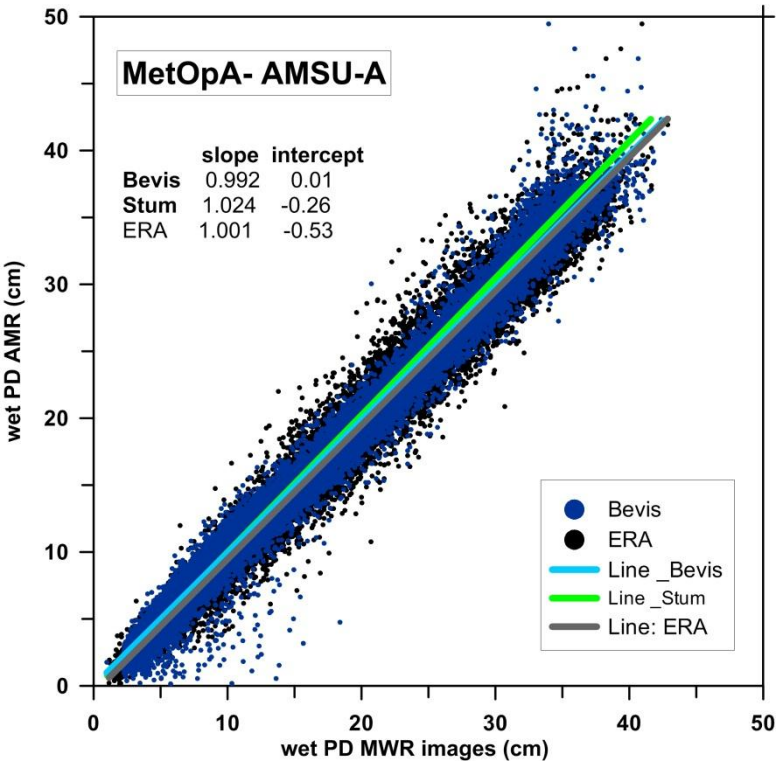

Figure 14. Wet path delay from AMR versus the corresponding values from MetOp-A/AMSU-A using the Bevis approach (blue). In black the corresponding values from ERA Interim. The solid lines represent the linear fit to each dataset.

Table 5. Calibration parameters (scale factor and offset) of the WPD_Bevis and WPD_Stum with respect to WPD_AMR (linear fits parameters), and RMS of the differences between these datasets before and after calibration.

Satellite	Solution type	Scale factor	Offset (cm)	RMS (cm) before / after	
AQUA	Bevis	0.980	-0.74	1.41	0.85
	Stum	1.012	-1.01	1.14	0.80
COR	Bevis	0.985	-0.71	1.33	0.88
	Stum	1.016	-0.97	1.11	0.86
F15	Bevis	0.986	-0.63	1.35	1.01
	Stum	1.018	-0.91	1.18	1.01
F16	Bevis	0.985	-0.63	1.34	0.98
	Stum	1.016	-0.89	1.16	0.97
F17	Bevis	0.982	-0.59	1.35	1.01
	Stum	1.012	-0.81	1.17	1.00
MTA	Bevis	0.992	0.01	1.14	1.13
	Stum	1.024	-0.26	1.09	1.06
N15	Bevis	0.999	0.12	1.22	1,21
	Stum	1.032	-0.18	1.23	1.15
N16	Bevis	0.997	0. 10	1.14	1.14
	Stum	1.029	-0.17	1.14	1.07
N17	Bevis	0.978	0.13	1.24	1.20
	Stum	1.010	-0.14	1.13	1.13
N18	Bevis	0.996	-0.09	1.20	1.19
	Stum	1.029	-0.37	1.13	1.10
N19	Bevis	0.993	0.06	1.17	1.17
	Stum	1.026	-0.21	1.12	1.08
TRM	Bevis	1.004	-0. 93	1. 38	1. 09
	Stum	1.041	-1.40	1.21	1.09

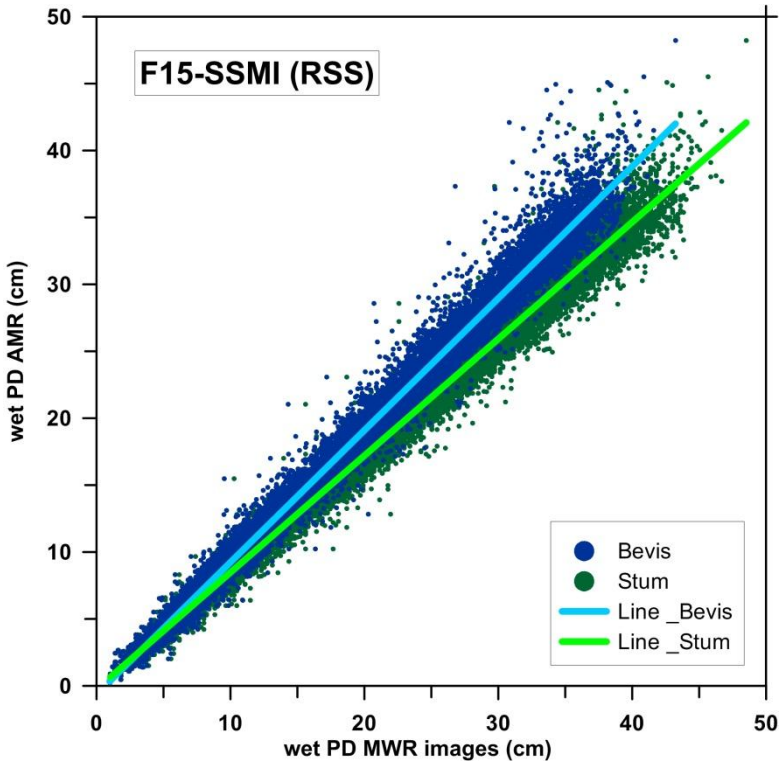

Figure 15. Wet path delay from AMR versus the corresponding values from DMSP-F15/SSMI (data from RSS) using the Bevis (blue) and the Stum (green) approaches. The solid lines represent the linear fit to each dataset.

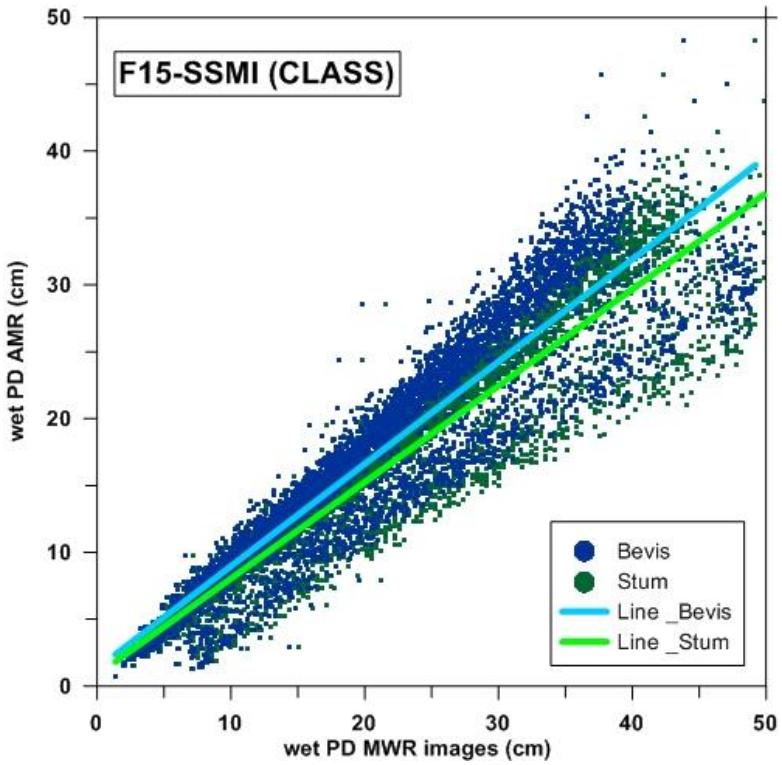

Figure 16. Wet path delay from AMR versus the corresponding values from DMSP-F15/SSMI (data from CLASS) using the Bevis (blue) and the Stum (green) approaches. The solid lines represent the linear fit to each dataset.

5. WTC estimation from ERA Interim

The ERA Interim (ECMWF ReAnalysis) model provides global grids of TCWV and surface temperature (2 metre Temperature, 2T) at 0.75°× 0.75° spacing and 6 hour intervals. From these single-level fields, at each grid node, the wet tropospheric correction for altimeter measurements can be computed from TCWV and 2T using Equation (1) and Equation (2).

Aiming to identify the most suitable NWM for use in the DComb algorithm, the WTC computed both from ERA Interim and ECMWF operational models, for the period of the three reference altimetric missions (TOPEX/Poseidon, Jason-1 and Jason-2) were compared, using the model values present in RADS. Results are shown in Figure 17, in which the statistical parameters (mean and standard deviation of the differences) for each mission cycle are plotted.

It can be observed that, since 1992, the operational model suffered various updates which originate discontinuities in the derived WTC. The mean differences between the two models reveal large discontinuities in the 90's.

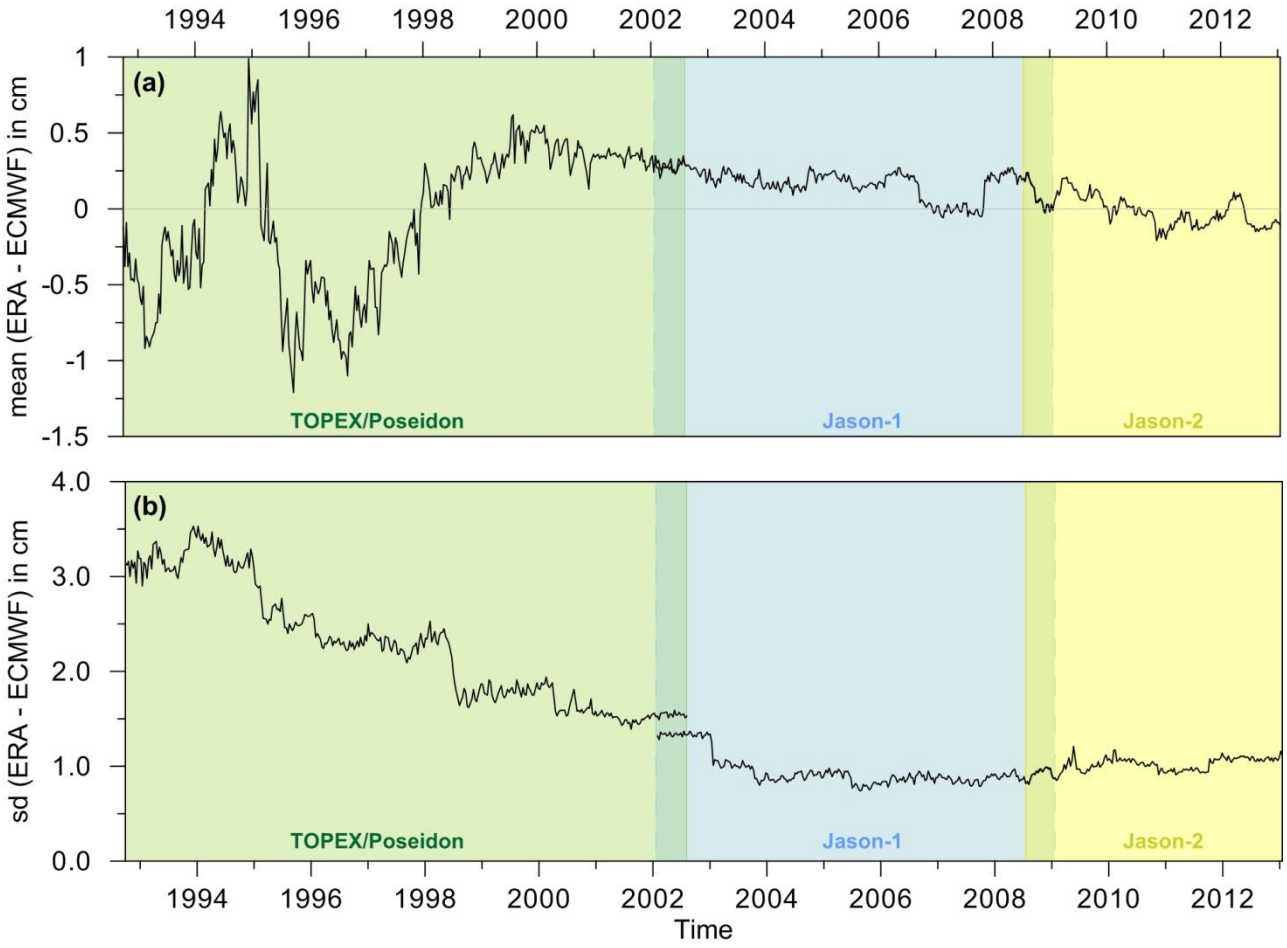

Figure 17. (a) Mean and (b) standard deviation (sd) of the differences between the WTC computed from ERA Interim and the ECMWF operational model (in cm) for each cycle of the three reference altimetric missions: T/P, J1 and J2.

Figure 17(b) shows that the standard deviation of the differences between the two models decreases from about 3 cm in the early 90's to about 1 cm since 2004. Comparisons (not shown here) between each model and the WTC derived from the measurements of the microwave radiometer on board each altimetric mission show that both models agree with the MWR derived WTC within 1.1 1.2 cm (1 standard deviation).

In summary, results show that ECMWF operational model is not suitable for use in altimetric studies requiring centimetre level accuracy. Since about 2004, the accuracy of ERA Interim model is similar to present ECMWF operational model and has the advantage of being homogeneous through time [*Dee et al.*, 2011]. Consequently, ERA Interim has been identified as the most appropriate model for use in the DComb algorithm.

6. The DComb algorithm – status of implementation

The main steps involving the computation of an improved WTC for CS-2 are:

(1) Inter-calibration of all existing data types, in particular those from all scanning radiometers on board remote sensing missions using the Advanced Microwave Radiometer (AMR) on board Jason-2 and the ERA Interim model;

(2) implementation of the DComb algorithm by Objective Analysis (OA) of all existing data types;

(3) global computation of WTC for along-track data (1 Hz, interpolated to 20 Hz) -- positions as in RADS and in orbit files provided by ESA.

The first step is mostly concluded and reported in this document (section 4). The remaining steps involve the inter-comparison of GNSS- with AMR-derived WTC. A similar study has been previously performed in the scope of COASTALT and needs to be updated using the current GDR-D version of AMR.

An overview of the current implementation of the DComb algorithm is now presented. The wet tropospheric correction derived from the MWR on board altimetric missions is usually an invalid value for points in the coastal and polar regions due to land and ice contamination respectively. The GNSS-derived path delay (GPD) algorithm has been designed to tackle the problem of land contamination in the MWR measurements [*Fernandes et al.*, 2010]. The invalid MWR values are replaced by those estimated by the GPD algorithm, which consists in a data combination methodology using linear space–time objective analysis. The combination of zenith wet delay values from independent and different sources (e.g., tropospheric delays from either GNSS stations or numerical weather models, and valid radiometer measurements from onboard altimetric missions) takes into account the accuracy of each available data set and the spatial and temporal variability of the WTC field. Simultaneously, it calculates the error associated with each estimate.

Amongst others, one of the advantages of the methodology is that it can be applied to estimate the value of any field at any location, provided that samples from that field are available with an appropriate spatial and temporal distribution. In particular, the GPD methodology is adequate to calculate the wet tropospheric correction for the CS-2 mission. In the absence of onboard MWR measurements, the methodology shall rely mostly on the WTC derived from the large data set of SI-MWR TCWV products, on the tropospheric delays derived from the GNSS stations and from numerical weather models such as ERA Interim. Basically, the algorithm for estimating the WTC for CS-2 – the DComb methodology – can be regarded as an upgrade of the GPD algorithm.

The DComb algorithm is under development, the use of data from scanning radiometers being currently implemented.

7. Summary and future work

In this document the status of the task involving the computation of an improved WTC for CS-2 has been described. The focus is on the analysis of the water vapour dataset of SI-MWR sensors available for the computation of the WTC for CryoSat-2. In the scope of CP4O WP4000, the next step consists in finishing the implementation of the data combination algorithm (DComb) using, amongst others, the inter-calibrated datasets described in sections 4 and 5.

It has been shown in section 4 that water vapour images from MWR on board RS missions constitute a very valuable dataset for the computation of WTC, particularly favourable for the CS-2 mission due to its orbital characteristics with respect to those of the considered RS satellites. There are at present 10 RS missions in near polar sun-synchronous orbits providing water vapour products: NOAA-15, -16, -17, -18, -19, MetOp-A, DMSP-F15 (with some restrictions), -F16, -F17 and Coriolis. Data from AQUA mission was not taken into account, since AMSR-E stopped working on early October 2011, but it is also expected that DMSP-F18 products shall be released soon. In addition, there is also the low inclination TRMM mission providing TCWV data in the latitude band ±40°. In summary, since October 2011 there is a total of 11 satellites, with five different MWR scanning sensors with variable pixel size: 50 km, 25 km and 10 km (for nadir looking).

The analysis performed so far, with all the available (and reliable) data, show that for CS-2 the space-time coverage of the available SI-MWR TCWV images varies with time and, consequently, also that of the derived WTC. In contrast to periods for which full coverage is attained within two to three hours, for the less favourable periods about 10% of the CS-2 measurements over a sub-cycle time span will have no images available within three hours (for a distance up to 75 km), thus relying on NWM-derived WTC or the availability of GNSS data (near the coast). This stresses the importance of these two other datasets to be used in DComb: GNSS-derived WTC data and the best available NWM -- which at present and for global studies, is the most recent reanalysis model from ECMWF (ERA Interim).

Coastal Ocean areas shall greatly benefit from the use of GNSS-derived WTC (computed at land-based, coastal or island, GNSS stations), due to the general unavailability of valid MWR measurements at short distances from the coast. In these regions, GNSS data is a crucial WTC data source, available online from various networks, e.g. IGS (International GNSS Service), EPN (EUREF Permanent Network) and United States SuomiNet. It has been shown [*Fernandes et al.*, 2010; *Fernandes et al.*, 2013] that the most recent GNSS processing techniques lead to accurate (better than 1 cm) ZWD estimates which are stable in time, i.e., show no drift with respect to ERA Interim. The GNSS-derived path delays will be instrumental in the computation of the WTC in the coastal zones, for the full exploitation of the CS-2 SAR measurement mode.

For Open Ocean areas, the main data source shall be SI-MWR-derived WTC and also ERA Interim for epochs/locations with low SI-MWR data coverage. For Polar Ocean regions, generally with sparse GNSS coverage and some SI-MWR data flagged as invalid due to sea-ice contamination, improvements to present ECMWF WTC are expected to be more modest.

As previously reported in D2.2 – Development and Validation Plan, and considering the availability of independent data for the validation of the derived DComb WTC, the proposed validation

methodologies will vary according to the domain (or sub-theme). For Open Ocean, as the main data source will be the SI-MWR-derived WTC, and no absolute standard is yet available for spaceborne MWR, the validation shall be performed by comparing DComb-derived WTC with WTC from a chosen reference MWR (e.g. AMR on board Jason-2). As far as Coastal Ocean is concerned, DComb outputs will be subject to comparison with independent -- not used in the objective analysis computations -- GNSS-derived WTC. A global analysis of sea level anomaly (SLA) variance at crossovers, after use of the DComb WTC data, shall provide an indicator of the performance of DComb with respect to the currently provided ECMWF WTC, with emphasis on latitudinal and coastal -- distance from coast -- dependencies.

References

Bevis, M., S. Businger, S. Chiswell, T. A. Herring, R. A. Anthes, C. Rocken, and R. H. Ware (1994), GPS METEOROLOGY - MAPPING ZENITH WET DELAYS ONTO PRECIPITABLE WATER, *Journal of Applied Meteorology*, *33*(3), 379-386, doi:10.1175/1520-0450(1994)033<0379:gmmzwd>2.0.co;2.

Brown, S. (2013), Maintaining the Long-Term Calibration of the Jason-2/OSTM Advanced Microwave Radiometer Through Intersatellite Calibration, *IEEE Trans. Geosci. Remote Sensing*, *51*(3), 1531-1543, doi:10.1109/tgrs.2012.2213262.

Cao, C. Y., R. Y. Chen, and L. Miller (2011), Monitoring the Jason-2/AMR Stability Using SNO Observations from AMSU on MetOp-A, *Marine Geodesy*, *34*(3-4), 431-446, doi:10.1080/01490419.2011.584829.

Dee, D. P., et al. (2011), The ERA-Interim reanalysis: configuration and performance of the data assimilation system, *Quarterly Journal of the Royal Meteorological Society*, *137*(656), 553-597, doi:10.1002/qj.828.

Fernandes, M. J., C. Lazaro, A. L. Nunes, N. Pires, L. Bastos, and V. B. Mendes (2010), GNSS-Derived Path Delay: An Approach to Compute the Wet Tropospheric Correction for Coastal Altimetry, *Ieee Geoscience and Remote Sensing Letters*, *7*(3), 596-600, doi:10.1109/lgrs.2010.2042425.

Fernandes, M. J., N. Pires, C. Lázaro, and A. L. Nunes (2013), Tropospheric Delays from GNSS for Application in Coastal Altimetry, *Advances in Space Research*, *51*(8), doi:10.1016/j.asr.2012.04.025.

Ignatov, A., I. Laszlo, E. D. Harrod, K. B. Kidwell, and G. P. Goodrum (2004), Equator crossing times for NOAA, ERS and EOS sun-synchronous satellites, *International Journal of Remote Sensing*, *25*(23), 5255-5266, doi:10.1080/01431160410001712981.

Keihm, S. J., M. A. Janssen, and C. S. Ruf (1995), TOPEX/POSEIDON MICROWAVE RADIOMETER (TMR) .3. WET TROPOSPHERE RANGE CORRECTION ALGORITHM AND PRE-LAUNCH ERROR BUDGET, *IEEE Trans. Geosci. Remote Sensing*, *33*(1), 147-161, doi:10.1109/36.368213.

Keihm, S. J., V. Zlotnicki, and C. S. Ruf (2000), TOPEX Microwave Radiometer performance evaluation, 1992-1998, *IEEE Trans. Geosci. Remote Sensing*, *38*(3), 1379-1386, doi:10.1109/36.843032.

Mendes, V. B., G. Prates, L. Santos, and R. B. Langley (2000), An evaluation of the accuracy of models of the determination of the weighted mean temperature of the atmosphere. , *In: Proceedings of "ION 2000 National Technical Meeting", Anaheim, CA.*

Miller, M., R. Buizza, J. Haseler, M. Hortal, P. Janssen, and A. Untch (2010), Increased resolution in the ECMWF deterministic and ensemble prediction systems., *ECMWF Newsletter*, *124*, 10-16.

Stum, J., P. Sicard, L. Carrere, and J. Lambin (2011), Using Objective Analysis of Scanning Radiometer Measurements to Compute the Water Vapor Path Delay for Altimetry, *IEEE Trans. Geosci. Remote Sensing*, *49*(9), 3211-3224, doi:10.1109/tgrs.2011.2104967.